PCCP

Expansion dynamics and chemistry evolution in ultrafast laser filament produced plasmas

Journal:	*Physical Chemistry Chemical Physics*
Manuscript ID	CP-ART-01-2020-000078.R1
Article Type:	Paper
Date Submitted by the Author:	06-Mar-2020
Complete List of Authors:	Kautz, Elizabeth; Pacific Northwest National Laboratory, National Security Directorate Yeak, Jeremy; Opticslah Bernacki, Bruce; Pacific Northwest National Lab, Phillips, Mark; University of Arizona, Optics Science Center; Opticslah Harilal, Sivanandan; Pacific Northwest National Laboratory, National Security

ARTICLE

Expansion dynamics and chemistry evolution in ultrafast laser filament produced plasmas

Received 00th January 20xx,
Accepted 00th January 20xx

DOI: 10.1039/x0xx00000x

Elizabeth J. Kautz,[a] Jeremy Yeak,[b] Bruce E. Bernacki,[a] Mark C. Phillips,[b,c] and Sivanandan S. Harilal*[a]

Laser ablation in conjunction with optical emission spectroscopy is a potential non-contact, standoff detection method for all elements in the periodic table and certain isotopes such as radionuclides. Currently, significant development efforts are on-going to use ultrafast laser filaments for remote detection of materials. The application of filaments is of particular interest in extending the range of stand-off capability associated with elemental and isotopic detection via laser-induced breakdown spectroscopy. In this study, we characterize the expansion dynamics and chemical evolution of filament-produced uranium (U) plasmas. Laser filaments are generated in the laboratory by loosely focusing 35 femtosecond (fs), 6 milli Joule (mJ) pulses in air. Two-dimensional spectrally-integrated and time-resolved imaging was performed to study hydrodynamics and evolution of U atomic and UO molecular emission in filament-produced U plasmas. Our results highlight that filament ablation of U plasmas gives a cylindrical plasma plume morphology with an appearance of plume splitting into slow and fast moving components at later times of its evolution. Emission from the slow-moving region shows no distinct spectral features (i.e. broadband-like) and is contributed in part by nanoparticles generated during ultrafast laser ablation. Additionally, we find U atoms and U oxide molecules (i.e. UO, U_xO_y) co-exist in the filament produced plasma, which can be attributed to the generation of low-temperature plasma conditions during filament ablation.

Introduction

Optical emission spectroscopy (OES) of a laser-produced plasma (LPP), commonly called laser-induced breakdown spectroscopy (LIBS), is a well-established technique for elemental and isotopic detection.[1, 2] LIBS is a rapid, all-optical method that requires no sample preparation, and has demonstrated sensing capabilities for stand-off distances from tens to ~100 meters.[2, 3] Thus, LIBS is of interest for remote analysis of actinide-bearing materials, such as uranium (U), for nuclear forensics, safeguards, security and treaty verification applications.[3-5] LIBS is also utilized for remote sensing in the Mars rover where the detection range is ~7 m.[6] Furthermore, OES of laser-produced plasmas is utilized as a lab-scale testbed for improved understanding of fireball explosion, plasma chemistry, and debris generation in an explosion event.[3, 7, 8] Despite the technique's many benefits and application areas, there are still several challenges that exist for using LIBS for remote detection at large standoff distances (≥ 100 meters). Specifically, the delivery of sufficient laser energy for efficient target ablation and the collection of enough light (which has a $1/r^2$ dependence) for analysis to obtain good signal to noise ratio are particularly significant challenges. To overcome such challenges, laser beam delivery at standoff distances and plume emission properties require further study.[3]

The emission signature from any LPP plume is influenced by multiple factors, including plasma and target material properties,[9] and plasma generation conditions.[10, 11] Plasma properties (e.g. temperature, hydrodynamics, densities of electrons, ions, and atoms) are directly coupled to plasma generation conditions (laser wavelength, laser spot size, intensity, pulse width, etc.) as well as target properties (atomic weight, number density, etc.). Gas-phase chemistry also influences the target material of interest if it undergoes combustion in air, which is the case for pyrophoric metals (e.g. U, Al, Pu). Pulsed nanosecond (ns) laser systems (e.g. Q-switched Nd:YAG lasers) have been used extensively for stand-off analysis of LIBS of various material systems, including U.[3] Plasmas produced by short pulse duration (e.g. femtosecond) lasers have several characteristics that differ from longer duration (e.g. ns) pulsed laser systems, such as: generation of cooler plasma, improved ablation efficiency, smaller heat-affected zones in the target material, negligible laser-plasma coupling and Bremsstrahlung emission, and reduced elemental fractionation.[12-17] Femtosecond (fs) laser ablation produces a plasma plume that is primarily comprised of atomic species, which is favourable for molecular formation.[18] Both atomic and molecular emission within an ultrafast laser-produced U plasma can be used for remote analysis of elements and isotopes in U-bearing materials.[3, 19, 20]

When an ultrafast laser pulse undergoes self-focusing via nonlinear Kerr effect during its propagation in a transparent medium (such as air), a weakly ionized plasma is generated. The

[a] Pacific Northwest National Laboratory, Richland, WA 99352 USA
[b] Opticslah, LLC, Albuquerque, NM 87106, USA
[c] James C. Wyant College of Optical Sciences, University of Arizona Tucson, AZ 85721, USA
*Corresponding Author: sivanandan.harilal@pnnl.gov

generated plasma possesses a negative refractive index (because of the electron cloud) which acts as a diverging medium and therefore decreases the intensity of the propagating beam. The equilibrium between focusing and defocusing of the ultrafast laser beam leads to the formation of filaments. Filaments carry a small fraction of laser energy (~10 %) and the remaining energy appears as a reservoir or a photon bath surrounding the filament.

Currently, there is a significant interest in using ultrafast laser generated filaments for remote analysis of atmospheric gases, aerosols, elements, and isotopes.[21, 22] Filament-based analysis is attractive for remote detection because ultrafast laser propagation to large distances (i.e. hundreds to thousands of meters[23-25]) can be achieved without diffraction effects due to self-focusing and subsequent filament generation. The filament formation distance, and thus standoff distance, can be controlled by varying the initial laser chirp and external focusing conditions. In reality, the peak intensity available for ablation from fs laser pulses in atmospheric conditions is limited due to intensity clamping.[26] It has also been reported that even under strong external focusing conditions using a shorter focal length lens, the intensity clamping effect still plays a significant role.[27] Under these conditions, the peak intensities may exceed the clamping intensity value by at least one order of magnitude.[28] The ablation efficiency, as well as the temperature of the filament ablated plumes, are lower compared to plasmas produced by ns and focused fs laser pulses,[29, 30] and hence shock waves formed during filament ablation may be weaker.

For LIBS applications, extending the detection range using ns lasers is problematic because of beam diffraction effects. Filaments formed during ultrafast laser propagation has been suggested to overcome this limitation and can be used for generating LIBS plumes at large stand-off distances. Self-guided filaments possess a peak intensity of ~5×10^{13} Wcm^{-2}, which is powerful enough for the ablation of any target material. However, limited studies have been carried out on understanding the dynamics and chemistry of filament generated plasmas, which is essential for optimizing this technique for future standoff detection applications.

Filaments during ultrafast laser propagation are routinely generated using two approaches: (1) propagating the beam to large distances where self-focusing leads to the collapse of the beam, and (2) use of a long focal length lens for generating filaments in a laboratory setting.[30] For long-range standoff applications, filaments should be generated using the former method, where the filament formation distance can be manipulated by adjusting the laser chirp. For laboratory-based filament generation, a long focal length lens is used for loosely focusing the laser beam to control the onset of filamentation to a certain distance as dictated by laboratory size and set-up. Previous studies showed that filament generation conditions affect properties of ablation plumes, which were attributed to the efficient use of the energy reservoir surrounding the filament for plasma generation.[30] The use of higher laser intensity may lead to the formation of multiple filaments during its propagation, which may also affect the properties of subsequently generated ablation plumes. Hence, the filament generation conditions ultimately determine the number of filaments, intensity, electron plasma density, and geometry of the energy reservoir around the filament. All these factors then affect the dynamics of plasmas generated by filament ablation and hence its optical emission properties.

Although fs-filamentation is a promising technique for standoff detection of U-bearing materials, there is currently a lack of understanding regarding plume dynamics, morphology, and chemistry of filament-produced U plasmas. While the interplay between plume expansion and chemistry are well characterized for a ns-LPP in our prior work,[31, 32] such phenomena in a fs- or filament-ablation system have not yet been explored for the U system, which is a prerequisite for using filaments for remote detection of actinides. Here, we explore fundamentals of plasma chemistry evolution in a plasma produced via filament LA in air at approximately atmospheric pressure from a metallic U target. We characterize the spatio-temporal expansion dynamics and chemical evolution of filament-ablated U plasmas. Ultrafast laser filaments are generated in the laboratory by loosely focusing 35 fs, 6 mJ pulses in air. Fast-gated imaging was performed to evaluate plume expansion dynamics, and 2D spectral imaging was used to study the spatially and temporally resolved emission dynamics of U atoms and U oxide molecules (e.g. UO, U_xO_y).

Experimental Details

A fs Ti:Sapphire laser system (Coherent Astrella) with ~ 800 nm wavelength and ~35 fs full width half maximum (FWHM) pulse width was operated at 10 Hz for generating filaments in a laboratory setting. An anti-reflection coated plano-convex lens with *f*=1 m was used to generate filaments in air. The laser energy used for filament generation was 6.2 mJ (or a peak power of ~177 GW). A schematic of the experimental set-up used in this work is shown in Figure 1(a). Using a *f*=1 m lens, filaments were formed at ~93 cm from the focusing lens and having an elongation of ~ 8 cm, as shown in Figure 1(b). The target material for ablation was a natural U metal sample (0.7%

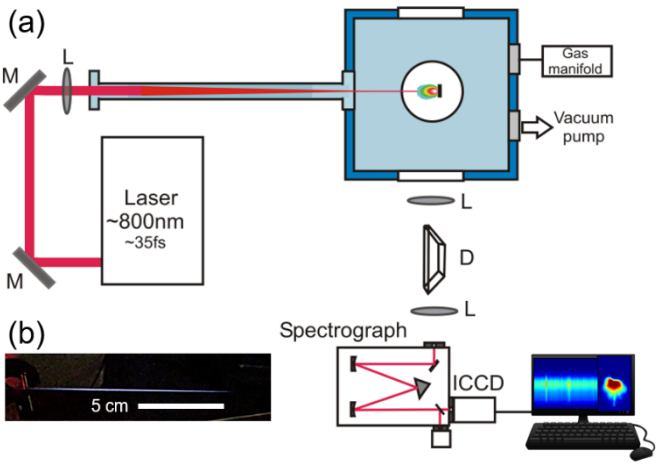

Fig. 1 (a) Experimental set-up used for collecting 2D spectrally-integrated and resolved plasma images, and (b) photograph of a filament produced in air. Acronyms above are defined as follows: M – mirror, L – lens, D – dove prism, ICCD – intensified charged coupled device.

^{235}U and 99.3% ^{238}U). The target was housed in a cubic vacuum chamber (0.125 ft^3 volume), used for trapping particles generated during LA. The chamber was attached to a dry scroll pump and a gas manifold for pressure and ambient gas control. For this work, the chamber was filled with air, and kept at 700 Torr pressure.

The vacuum chamber was equipped with optical windows for laser ablation and light collection, and pressure gauges to allow for monitoring chamber pressure. To avoid filament-induced optical damage to the laser entrance window, a ~70 cm vacuum nipple was attached to the chamber. In this configuration, the front window of the vacuum nipple was ~78 cm away from the target position to prevent window damage. The vacuum chamber was fixed to an *x-y-z* translator stage so that the target position could be easily changed to avoid target drilling.

An optical system consisting of two plano-convex lenses was used to image the plasma plume onto the slit of a 0.5m Czerny-Turner spectrograph (Acton Spectrapro 2500i). The plume was imaged such that the plume expansion direction was parallel to the slit height with the help of a Dove prism.[33] The spectrograph was coupled to an intensified charged coupled device (ICCD) camera (PIMAX4, 1024 × 1024 pixels) for recording time-resolved 2D spectral images. The measured spectral resolution using a He-Ne laser with a 30 µm slit was ~40 pm. The spectrograph and ICCD were positioned orthogonal to the plasma expansion direction. Time-resolved, spectrally integrated plume images were recorded by operating the spectrograph grating as a mirror. To operate the grating in this manner, the zeroth-order reflection was used and the maximum entrance slit (~3 mm) was used. A 2400 grooves/mm holographic grating optimized for the visible spectral regime was used for recording the 2D spatially-resolved, wavelength dispersed images. For recording broad spectral features of U plasma in the visible spectral region (400-650 nm), light emitted from the plasma was collected with a lens and focused to a 400 µm multimode fiber. This fiber was coupled to a 0.3 nm spectrograph (Isoplane). For recording spectral features, 1200 grooves/mm or 150 grooves/mm gratings was used. The ICCD was synchronized with laser pulsing via a programmable timing generator.

Results

During ultrafast laser propagation in air, filaments are formed when the power of the laser is greater than the critical power (P_{cr}) for self-focusing.[21] Here, λ ~800 nm corresponds to a critical power for filament formation of ~3 GW. With laser parameters and optics (*f*=1 m lens) used in the present work, we observe a single filament produced in air. Previous studies showed that the ablation efficiency may change significantly with position of the target with respect to the filament channel produced in the laboratory frame.[30] We positioned the U target at ~ 93 cm from the focusing lens where the emission from the filament ablated plasma was found to be the brightest at atmospheric conditions. Our previous work showed that[26] the emission intensity of filament ablation plumes changes along the filament channel and found to be optimal approximately at the centre position along the filament channel.

Plasma Expansion Dynamics

The spatio-temporal evolution of filament-generated plasmas was investigated via 2D fast-gated plasma plume imaging, with representative images shown in Figure 2 for various times after plasma onset. The U plasma images were taken orthogonal to the plasma expansion direction at 700 Torr air pressure. A false colormap was applied to each image, which was normalized to its maximum intensity for obtaining high contrast. The sequence of images given in Figure 2 shows several morphological changes as a function of time after plasma onset. At early times (~1 µs), the plasma is located close to the target surface and has an approximately spherical shape. This morphology indicates the plume is expanding equally in all directions. As time increases (~3-5 µs), the approximately spherical plasma plume moves further from the target. Up to ~5 µs, the plume retains this spherical shape, and at later times (≥10 µs), the plasma becomes elongated, with a more cylindrical shape. Then, at ≥20 µs plume splitting is observed, where the plume is separated into faster and slower moving components. As the plume propagates at times >25 µs, the intensity of the faster component decreases. The plasma images provided in Figure 2 illustrate this rapid decay in the fast component

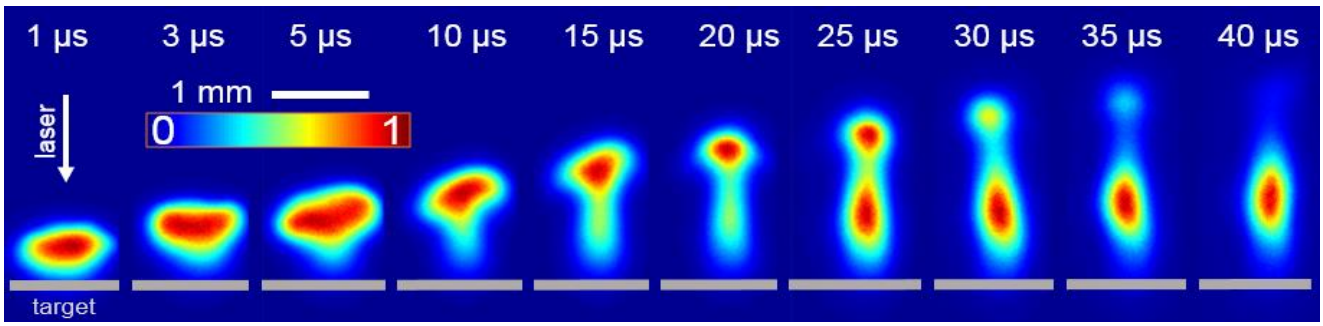

Fig. 2 Spectrally-integrated and fast-gated imaging of a U plasma plume produced by filament LA in 700 Torr air. Gate delay times are indicated above each plasma image. A progressive gate width (10 ns – 200 ns) was used to account for decreasing emission intensity from 1 to 40 µs. Each image is from a single laser shot and was normalized to its maximum intensity, and displayed with a false colour map. The direction of the incident laser is indicated with a white arrow, and the target position is shown with a grey rectangle in each image.

intensity, where at later times the slow component becomes prominent due to the intensity normalization.

Intensity along the plasma expansion direction at different distances from the target was also analyzed to understand plasma expansion dynamics. Representative intensity versus distance plots for various times after plasma onset is provided in Figure 3. The times after plasma onset analyzed in the Figure 3 plots correspond to the plasma images presented in Figure 2. At early times, the intensity distribution is represented by a single peak, and the maximum intensity location is propagating away from the target due to plume expansion. The intensity profile also becomes broadened with increasing time from ~1-10 µs. At times ≥10 µs, a slower propagating intensity peak is seen between the plume front and the target position, indicating plume splitting (which can also be visualized in Figure 2 plume images). The maximum intensity of the faster moving component decreases as time progresses. At 25 µs, peak intensities become approximately equal (seen in the two maxima in the intensity versus distance plot). At ≥25 µs, the intensity of the faster peak decreases until the plume intensity distribution is a single peak closer to the target at very late times (~ 40 µs).

To quantitatively describe plume expansion for fast and slow-moving components, distance-time (R-t) plots were generated from Figure 2 plasma images, and are plotted in Figure 4. Fast and slow-moving components were fit with different models to describe plume propagation. The fast-moving component is fit with a blast wave model ($R \alpha t^{0.4}$),[34] whereas the slow-moving component follows a straight line fit ($R \alpha t^{1}$), with a propagation velocity of ~$1.22 \pm 0.01 \times 10^3$ cm/s. A representative plasma image is also given in Figure 4 in which slow and fast components of the plume are labeled.

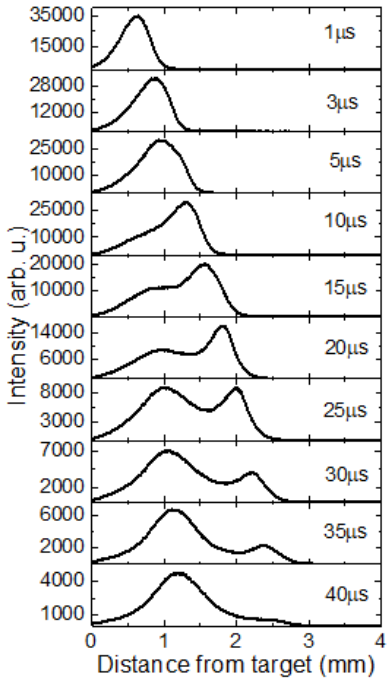

Fig. 3 Intensity versus distance from the target for a U plasma in 700 Torr air environment. Plots are provided for 1-40 µs after plasma onset. A progressive gating between 10 and 200 ns was used. Intensity values along the centreline emission zone (195 µm wide) of the plasma presented in the Figure 2 images were averaged to generate all intensity-distance profiles.

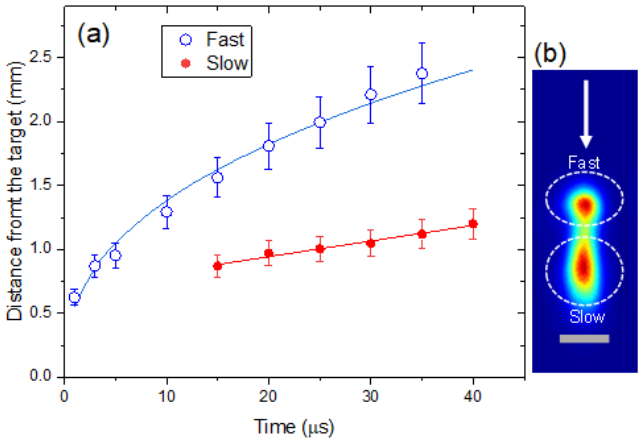

Fig. 4 (a) Distance from the target versus time (R-t) plots for fast and slow-moving components of the filament produced U plume. Each data point represents the maximum intensity from the corresponding spectrally integrated U plasma image. (b) Fast- and slow-moving regions are labelled on a plasma image taken at 25 µs from plasma onset. The incident laser direction is given by the white arrow and the target position is given by the grey rectangle. The solid lines in the figure correspond to blast wave (blue) and linear (red) fits.

When a U plasma is generated in air, the complex thermo- and plasma chemistry control emission features. Results presented in Figures 2-4 provide morphology and dynamics of the plasma, where all image data was spectrally-integrated over the wavelength range of 350-800 nm. Thus, no information regarding plasma chemistry can be obtained. Spectrally and time-resolved images are required to understand the evolution of plume chemistry during U plasma expansion in an oxygen-containing environment, such as air.

Plasma Chemistry Evolution

2D spectral imaging is a powerful diagnostic technique for evaluating plume chemistry, as they provide details of expansion dynamics of plume species, and spatial dependence of emission from atoms and molecules. For studying the evolution of U atoms and molecules within a filament produced U plasma in 700 Torr air, 2D spectral imaging was performed. A representative 2D spectral image is given in Figure 5(a) for the wavelength range of 590-596 nm at a delay time of 5 µs with a gate width of 2 µs. In this spectral region, the emission from U atoms (labelled as 'U I'), UO, and U_xO_y molecules (the broadband-like emission) co-exist within the plume.[35, 36] In Figure 5(a), the y-axis of the 2D spectral image provides the distance from the target. The spatial resolution in the 2D spectral images is dictated by the ICCD pixel size and magnification, and slit width for y and x axes, respectively. For 2D spectral images, each pixel in y (distance from the target) corresponds to 6.5 µm, and in x (wavelength) is 0.00617 nm. Figure 5(b) shows the spatial evolution of the emission spectra obtained from Figure 5(a). The emission intensity plotted in Figure 5(b) is weaker closer to the target, then gradually increases with increasing distance until a maximum intensity is reached at ~1.8 mm, after which intensity decreases sharply.

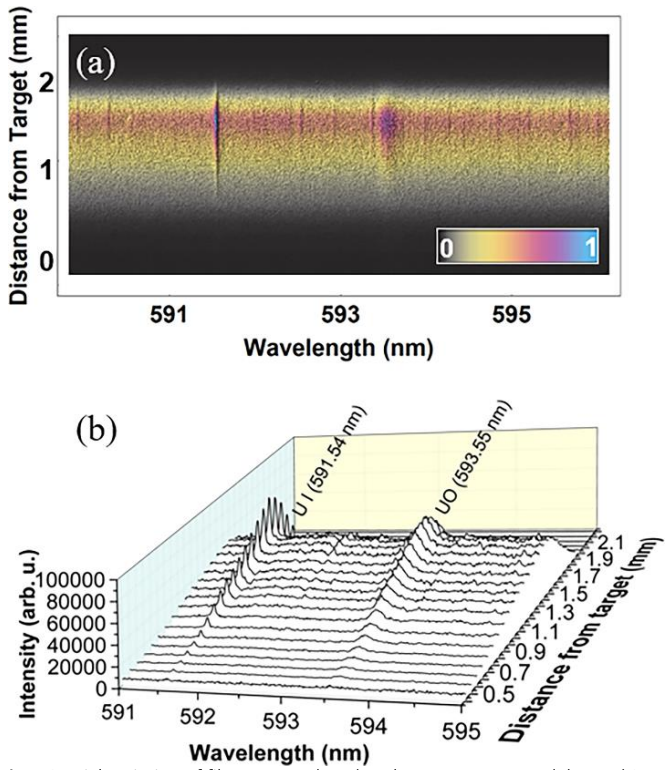

Fig. 5 Spatial variation of filament-produced U plasma at 5 μs gate delay and 2 μs gate width: (a) 2D spectral image, (b) spatially resolved spectral features corresponding to the 591-595 nm spectral image shown in (a). U I atomic and UO molecular peaks are labelled in (b). Each spectrum plotted in (b) is averaged over a 0.065 mm wide region from the 2D spectral image in (a).

The emission intensity of both U I and UO peaks follows the same trend.

To investigate the spatial and temporal evolution of oxidation in U plumes, and its relation to plasma hydrodynamics and confinement, 2D spectral images were recorded at 700 Torr air for various times after the onset of plasma formation, with results given in Figure 6. The spectral images show the movement of the emission zone away from the target with increasing time. At early times of plasma evolution (~200 ns), emission from the plasma appears very close to the target and U I lines are broadened, indicating higher plasma density. As time progresses, the strongest emission zone is moved further from the target as well as linewidths become narrower. At ~1 μs, the broad spectral features of UO at 593.55 nm are evident. At ~ 5 μs, the strongly emitting region has shifted close to the plume front, indicative of confinement effects. At time ≥ 11μs, two regions of optical emission zone are seen: one region further from the target, and one close to the target (which is initially weaker when compared to emission at the plume front). These regions correspond to the fast and slower-moving regions of the expanding plasma, previously presented in Figure 2 images. The relative intensities of the emission signal from the fast and slow-moving regions change as time progresses. At later times (≥30 μs), the emission from the slow-moving component is found to be stronger compared to the emission from the plume edges. Emission from the slow-moving region shows no distinct spectral features (i.e. broadband-like). The broadband-like emission from a laser-produced U plasma could be due to emission from polyatomic uranium oxides (U_xO_y) and/or from nanoparticles generated during ultrafast laser ablation.[37]

Horizontal cross-sections of the spectral images given in Figure 6 provide emission spectra at various distances from the target. Spectral features for the strongest emitting regions are presented in Figure 7, where sub-figure (a) is for earlier times in plasma evolution before plume splitting, and (b) presents spectra for later times in plasma evolution for both fast and slow-moving components in the split plume. Each spectrum was taken from the maximum intensity region of the 2D spectral image, which corresponds to regions 195 μm -325 μm (30-50 pixel) and 520 μm (80 pixels) wide for fast and slow components, respectively. The U plasma spectra in the wavelength range of 591-595nm (given in Figure 7) contains emission from U atoms, UO, and U_xO_y species. U I atomic emission lines in this region include a resonance transition at 591.54 nm (0–16 900 cm^{-1}), and a near-resonance line at 593.38 nm (620–17 468 cm^{-1}). Other prominent U I lines include: 592.55 nm (7646–24 517 cm^{-1}); 592.93 nm (3801–20 662 cm^{-1}); 594.28 nm (5762–22 585 cm^{-1}); and 594.86 nm (7646–24 452 cm^{-1}).

At early times (~100-500 ns), the emission is dominated by U I. The emission from UO molecular band at 593.55 nm is apparent at 1 μs. At ≥1 μs, the emission from UO species

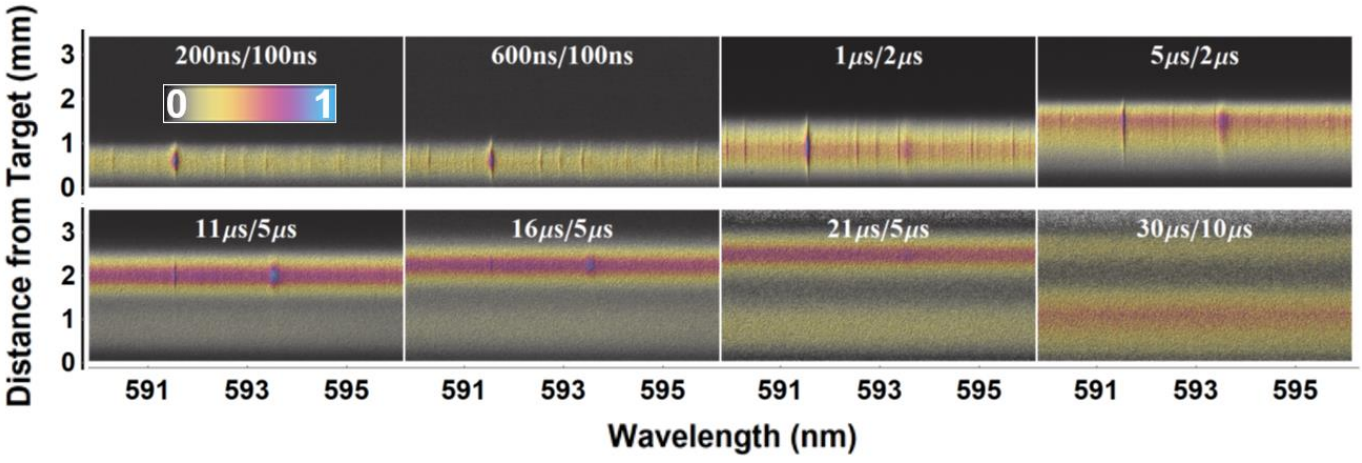

Fig. 6 Time-resolved 2D spectral images of filament-generated U plasmas in 700 Torr air. Each image represents the accumulation of 15 shots and represents spatially resolved emission features at the gate delay/width indicated on each plot. Each spectral image is normalized to its maximum intensity, with a false colour map applied.

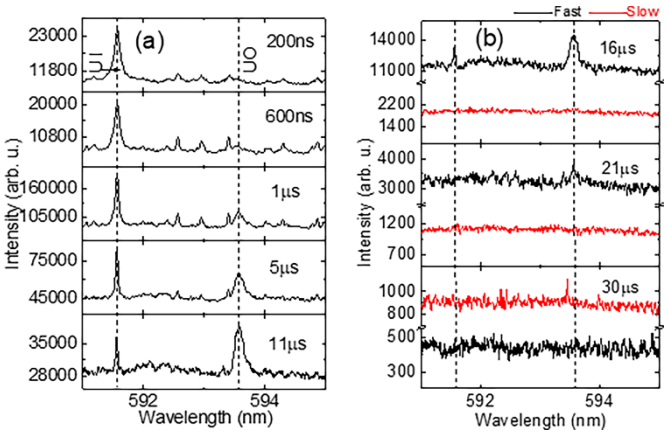

Fig. 7 Time and spatially resolved spectral features of U plasma evolution. Gate delay time is indicated on each plot. The following gate delay/gate widths were used to analyse emission signal at varying distances from the target to account for plume propagation: 200ns/100ns (0.5 mm), 600ns/100ns (0.6 mm), 1μs/2μs (0.9 mm), 5μs/2μs (1.6 mm), 11μs/5μs (2.0 mm), 16μs/5μs (fast – 2.2 mm, slow -0.6 mm), 21μs /5μs (fast- 2.4 mm, slow-0.5 mm), 30 μs /10 μs (fast-2.4 mm, slow – 0.8 mm). Spectral features were averaged over the region of maximum intensity in 2D spectral images. For the fast component, a 195-325 μm width region was used, and for the slower moving component, a 520 μm width region was used. Vertical dashed lines are provided as a guide to the eye for U I (591.54 nm) and UO (593.55 nm).

increases relative to U I. As time progresses, along with the emission from U I and UO, an apparent increase in background-like radiation is evident. At ≥16 μs, broadband-like emission dominates for both fast- and slow-moving components. Spectral features show the slow-moving component of the plume is only broadband-like, with no distinct peaks. At very late times (~ 30 μs), the emission from the slower moving region dominates (i.e. has higher intensity than the fast moving component). It is also noted here that the Figure 7 spectra at ~ 30 μs contains some noise spikes, but no distinct spectral features. Intensity for both components at this late time in plasma evolution is very weak in comparison to earlier times (< 16 μs). Additionally, linewidths of atomic and molecular emission change with space and time in a laser-generated plasma due to changes in temperature and density. The FWHM for U I (591.54 nm) at early times are broadened, then reaches the instrumental broadening limit (~40 pm) within 5 μs. UO (593.55 nm) peaks are broader than U I, with FWHM greater than 0.10 nm.

The spatio-temporal evolution of U I, UO, and broadband emission intensities will be useful for understanding the role of plume chemistry on emission dynamics. In order to evaluate the spatial variation of atomic and molecular species within the expanding plume at various times, intensity *versus* distance profiles were analysed for U I (591.54 nm), UO (593.55 nm) and broadband emission (593.10-593.16 nm) and results are given in Figure 8. For obtaining this plot, a narrow spectral bandwidth ~0.03 nm was used for the U I atomic transition at 591.54 nm, while a wider bandwidth ~ 0.06 nm was used for UO and broadband features to account for broader molecular emission. Since the broadband emission exists in the entire spectral region studied, the U I and UO intensities given are corrected for this broadband emission. Background correction was done by averaging broadband emission signal measured over the wavelength range of 593.10-593.16 nm (where no distinct spectral features are visible) and subtracting this value from U I and UO intensities.

Intensity *versus* distance profiles in Figure 8 illustrates that U I, and UO emission are stronger close to the target at ~1 μs and show somewhat similar trends. It is also noted that at early times of plasma evolution, and at closer distances from the target (≤1 mm), the spectral features may contain significant emission from continuum radiation which contributes background radiation. However, differences in the spatial evolution of emission from atoms and molecules are apparent at ≥ 5 μs. A sharp intensity decay at the plume front is observed for all intensity profiles at early times. At later times (≥ 10 μs), U I and UO intensity profiles become more symmetric (as compared to earlier times), and maximum intensity continues to move further from the target. At ~11 μs, a small secondary peak appears in the broadband profile close to the target. The intensity of this peak relative to the maximum peak increases at ≥11 μs. Simultaneously, U I and UO emission intensities decrease at times ≥ 11 μs.

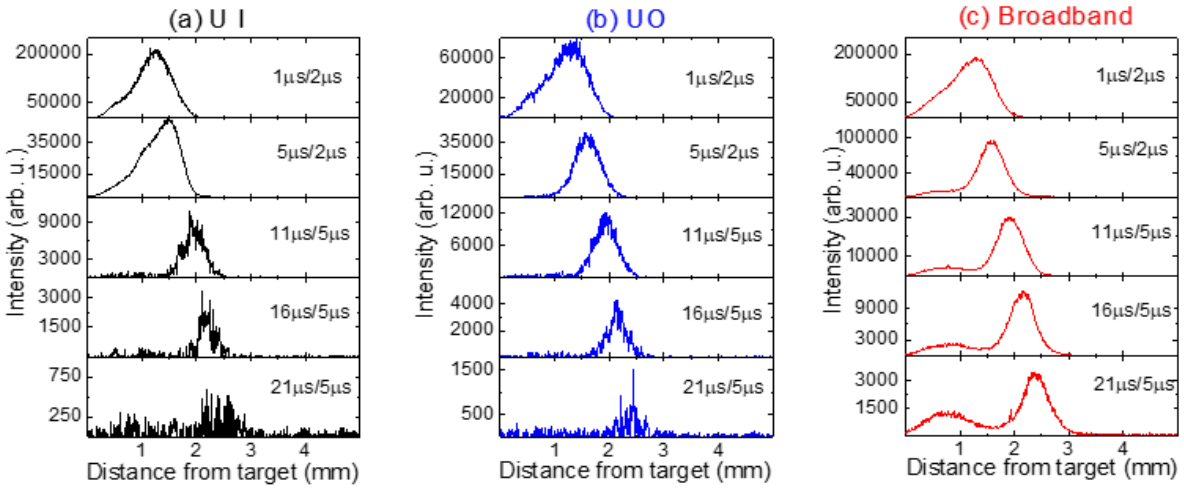

Fig. 8 Intensity versus distance for: (a) U I (591.54 nm), (b) UO (593.55 nm), and (c) broadband emission from 1-21 μs at 700 Torr pressure in air. Gate delays/gate widths are provided on each plot. All U I and UO data are corrected for the broadband emission. Intensity-distance profiles represent the intensity averaged over a ~0.06 mm width window for UO and broadband, and a ~0.03 mm width window for U I. The wavelength range used for broadband-like emission was 593.10-593.16 nm where no strong atomic or molecular peaks are observed.

In order to verify the source of broadband-like radiation in plume components, spatially-integrated and time-resolved emission features were recorded over a broad spectral range (400-650 nm) and results are given in Figure 9. The spectral features recoded at ~ 100 ns showed line radiation along with broadband which is due to continuum. At ~1 µs, the spectrum contains line radiation along with prominent broadband peaks around 480 nm and 595 nm which was previously identified as U_xO_y.[38] At 10 µs, most of the emission lines disappear, with the presence of broad spectral peaks. As time evolves (≥15 µs), the broad spectral features disappear gradually, and at ~35 µs a blackbody-type feature is apparent, suggesting the delayed component is primarily due to nanoparticle emission.

Discussion

Fast-gated, spectrally-integrated and spectrally-resolved imaging employing an ICCD is a well-known diagnostic tools for understanding morphology, hydrodynamics, and chemistry of the plasma plumes at all pressure levels.[39-41] The time-resolved plume images recorded at 700 Torr air pressure given in Figure 2 show rapid expansion at early times followed by confinement. We also observe a transformation from spherical to cylindrical plume morphology as time progresses, along with plume splitting at later times (≥15 µs). Collimation of fs LIBS plumes at atmospheric conditions has previously been reported in literature.[18, 42] Collimation is attributed to the narrower angular distribution of emitting species within a fs LPP in comparison to a ns-LPP, which could affect the confinement properties of the plume.[43] The focal length, as well as the position of the geometrical focal point of the focusing lens with respect to the target (in front, on, or behind the target), may also influence the laser-target coupling (and laser-plasma coupling in ns LPP).[44] The use of longer focal length lenses ($f \geq 50$ cm) in atmospheric conditions for generating fs LIBS plumes may lead to the formation of a filament channel, which impacts the LIBS plume hydrodynamics. Hence, the cylindrical column in atmospheric conditions seen during filament ablation could be due to the combined effects of directed particle emission and filament guided plasma flow.

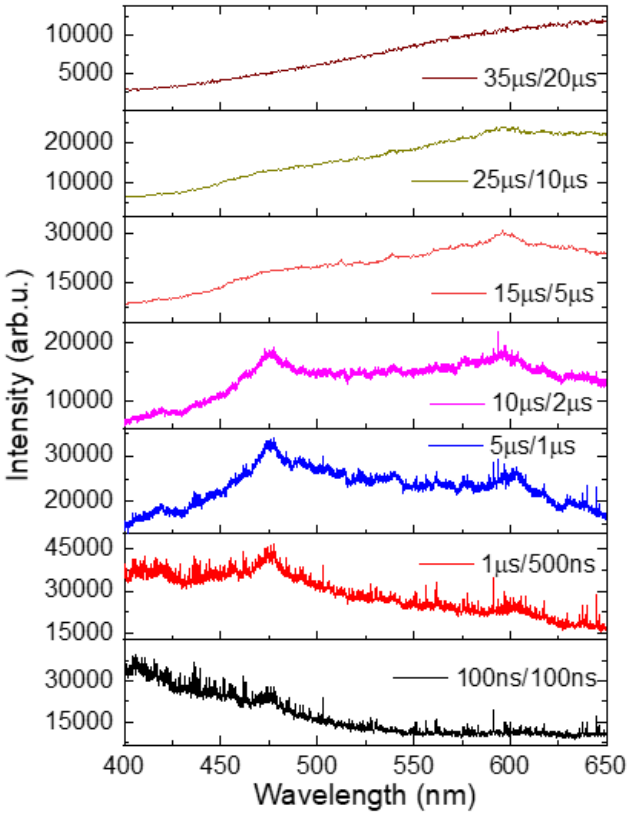

Fig. 9 Time-resolved, spatially-integrated broad spectral features of a filament produced U plasma in 700 Torr air, over the wavelength range of 400 – 650 nm. Gate delay/width is provided on each sub-plot. Spectra for gate delays of 100 ns to 10 µs were collected using a 1200 grooves/mm grating, and spectra for later times (15-35 µs) were collected using a 150 grooves/mm grating.

The results of plume imaging show that the elongated plume splits into components with two different velocities, evidenced by two peaks in the intensity *versus* distance profiles (Figure 3), where one component moves faster than the other. Plume splitting and elongation effects have been reported extensively for both ns[45] and ultrafast[40, 46] LPPs at vacuum and moderate pressure levels. Previous reports also showed that the plume splitting phenomenon strongly depended on laser spot size,[47] and cover gas pressure and chemistry.[38] Differences in velocities of plasma species (e.g. ions, neutrals) and the subsequent formation of an ambipolar electric field in the plume have previously been cited as one of the mechanisms leading to splitting.[41, 48, 49] Other potential reasons for plume splitting include generation of nanoparticles,[37] and delayed formation of molecules[50]. As shown in Figure 4, the fast-moving component seen in plume images experiences deceleration due to confinement and agrees with spherical blast wave theory[34] ($R \alpha t^{0.4}$). This expansion behaviour is typical for all laser-plasma systems at moderate to high background pressure levels.[51] The slow-moving component shows linear expansion behaviour ($R \alpha t$), which is similar to the free expansion of the plasma into a low-pressure ambient environment (e.g. vacuum). However, the measured velocities of the slow-component are in the subsonic regime (~12 m/s), which are much lower than free expansion velocity in vacuum or low-pressure environment. The vacuum free-expansion of LPPs typically propagate with high Mach numbers (≥ 100).[52] Significantly reduced velocities of the slower component indicates the presence of heavier molecules (U_xO_y) and/or nanoparticle by considering the relation between the velocity and mass of the species ($v \alpha M^{-1/2}$).

To investigate contributions of fast and slow moving components of the expanding plume, time-resolved 2D spectral imaging was performed. The 2D spectral images presented in Figure 6 show strong broadband-like radiation. Solid and gas-phase oxidation of U readily occurs in oxygen-containing environments, and is an active area of recent research in several fields (e.g. long-term storage of nuclear waste, nuclear forensics, and safeguards).[53, 54] U gas-phase oxidation is very complex, with several reaction mechanisms, including some of the prominent ones, such as: $U + O_2 \leftrightarrow UO + O$, $U + O_2 \leftrightarrow UO_2$, $UO_2 + O_2 \leftrightarrow UO_3 + O$.[55, 56] Through such reaction routes, U

monoxide (UO) and multiple higher oxide species can be produced (e.g. UO_2, UO_3, U_2O_2, U_2O_3, U_2O_4). Finko and Curreli[56, 57] documented favorable thermochemistry (12 channels) and plasma chemistry (17 channels) reaction pathways for the formation of U_xO_y. Plasma-ambient gas chemical reactions are known to be strongly influenced by the partial pressure of reactive species such as oxygen.[58] Such reactions lead to the formation of oxide species and a corresponding depletion of atomic species within the plume.[38] For the U system, previously reported research also demonstrated that the presence of oxygen in the ambient gas reduces the persistence of U plasma significantly. For example, U atomic emission persists for ≥ 100 μs in N_2 environment and is reduced to ≤ 20 μs in the presence of O_2.[38] However, tracking plasma chemistry using emission spectroscopy is a significant challenge, even for the simpler case of a steady-state plasma system.[59, 60] Considering the heterogeneous nature of a laser-plasma system (which has large gradients in temperature and density in both space and time),[61, 62] tracking the progression of U atoms to diatoms to heavy molecules is an intriguing problem.

Recently, significant attention has been devoted to understanding plume chemistry and molecular formation in ns-LA plumes for U and other metals.[31, 38] In our prior work, we used monochromatic, fast gated imaging for studying the evolution of U atoms and UO molecules in a ns-LPP, and found that U oxidation impacts plume morphology significantly, and depends strongly on oxygen partial pressure.[32] Emission spectroscopy combined with 2D spectral imaging is advantageous for tracking plume chemistry evolution as this approach provides spatio-temporal evolution of ions, atoms, and molecules within the evolving plume. In this work, the emission from atoms and molecules from filament generated U plasmas in 700 Torr changes with both space and time, as shown in Figures 5-7. Hotter conditions exist at early times in plasma evolution where continuum radiation dominates along with the emission from atoms and ions. When the plasma cools, the emission from atoms becomes more prominent, and molecular emission features (e.g. monoxide and higher oxides) appear at late times of plasma evolution when the temperature of the plasma is well below 10000 K. Our previous studies showed the favoured conditions for UO formation is at a plume temperature of ~1500-5000 K.[31]

Physical conditions within a transient plasma plume can impact spectral linewidth of measurements. Spectral lines are broadened due to various factors, including plasma conditions and detection system limitations (i.e. instrumental resolution). The major broadening mechanisms that influence the linewidths of atomic and molecular transitions include Stark, Doppler, and van Der Waals.[3] Linewidths of UO are significantly larger than U I due to overlapping unresolved lines. Each atomic and molecular species absorbs or emits light at a set of discrete, characteristic frequencies determined by the energy levels and their populations. Molecular species in particular will have an array of transitions due to the inclusion of vibrational and rotational energy levels. UO features seen in the present measurement can be considered as the convolution of numerous transitions. It should also be mentioned that for molecules with large moments of inertia (such as UO), the rotational levels become more closely spaced and may be difficult to resolve using standard emission-based passive techniques (e.g. LIBS) used in the present study. Extremely high resolution and active sensing spectroscopic tools such as laser absorption spectroscopy, laser-induced fluorescence, or frequency comb spectroscopy of plasmas[63] may be useful for resolving these finer structures of UO molecular emission.

The spatio-temporal variation U I, UO, and broadband emission features given in Figures 6-9 show the progression of atoms to diatoms and heavy polyatomic molecules in a U plasma at atmospheric conditions (700 Torr air). At early times, the emission from U plasma is dominated by the continuum along with emission from atoms and ions. The continuum emission in a laser-produced plasma is due to free-free (bremsstrahlung) and free-bound (radiative recombination) transitions because of the existence of higher electron temperature and electron and ion number density. In the case of U plasma, the continuum can also be caused by the high density of spectral lines. Due to rapid decay of electron temperature and density, the continuum emission from laser-produced plasmas persists only at early times (≤ 1 μs) and at closer distances to the target (≤ 1 mm). At all times, U I and UO are co-located within the plume, which can be attributed to the lower temperatures expected for filament-produced plasmas in comparison to ns-LPPs. In our prior work, we demonstrated clear spatial segregation between U I and UO in an expanding ns-LPP of a natural U target. UO was found to be formed further from the target, where cooler temperatures favoured molecular formation. [31, 32] However, in the present work we find a distinctly different spatial and temporal evolution of UO and higher oxides formed in plumes produced via filament LA. We find that up to 16 μs, U I, UO, and the maximum peak in the broadband emission are co-located within the expanding plume. After plume splitting, we find that the broadband emission intensity versus distance profiles (Figure 9) show double peaks, which are absent in the U I and UO profiles.

At later times (> 16 μs), the 2D spectral images of filament ablated plasma show no distinct spectral features, with only background-like radiation (Figures 6). From fast-gated images, and corresponding spectral features (Figure 7) and intensity *versus* distance profiles (Figure 8), we find a two-component plume morphology, where the slower component provides broadband emission with no distinct features. At early times, the faster moving component is contributed by both U I and UO (seen in the Figure 7 spectra). Previous studies showed U polyatomic oxide emits broad spectral features.[35, 38] However, the emission from nanoparticles could also lead to broadband emission features.[64] At early times of ultrafast laser ablation, the atomization is larger due to high temperature near the target surface, and ablation efficiency is lower as the heat diffusion towards the bulk is larger. At late times (> 15 μs), a nanoparticle plume is ejected from the target. The ejection of nanoparticles may be due to heat diffusion to the bulk where the deeper layers are not fully atomized, and instead are ejected in the form of nanoparticles. [66] The emission from a nanoparticle plume provides a blackbody curve.[37, 65] Thus, both

U_xO_y generated through plasma chemistry and nanoparticles produced during ultrafast laser ablation can provide broadband emission seen in Figure 6. However, the emission from U_xO_y provides distinct broad peak structures while a Planckian-type curve is expected from excited nanoparticles.

The time-resolved broad spectral features (400-650 nm) given in Figure 9 show a Planckian-type curve at late times of filament plume evolution indicating the emission at very late times is primarily contributed by nanoparticles. The plume images (Figure 2) also showed the emission from the slow-moving component dominates at very late times during its evolution which has a propagation velocity of ~$1.22 \pm 0.01 \times 10^3$ cm/s. This finding is consistent with reported nanoparticle plume velocity during ultrafast laser ablation.[37, 40] We also recorded plume morphology evolution via fast gated imaging of filament ablated U plasma in N_2 and Ar ambient gas environments at 700 Torr where gas-phase plume oxidation is expected to be absent. The plume splitting phenomenon seen in ambient air was also observed in both N_2 and Ar ambient, and these results confirm that the slower component seen in plume images are indeed contributed by nanoparticles. Hence, the broad spectral emission features seen closer to the target at delayed times are due to nanoparticles while that observed farther from the target in 2D spectral images (Figure 6) are contributed by U_xO_y.

Conclusions

We investigated the expansion dynamics as well as chemical evolution in a filament generated U plasma. Fast gated imaging and emission spectroscopy employing 2D spectrally- resolved imaging were used as diagnostic tools. Time-resolved imaging of filament ablation plumes showed an initially spherical plume that evolved into a cylindrical, elongated morphology with plume splitting at later times. The cylindrical shape of the filament ablated plume could be due to the combined effects of narrow angular distribution of emitting particles (typically seen in ultrafast LPPs), and filament guided plasma flow. The plume was found to split into fast and slow-moving components that followed blast wave and linear expansion models, respectively. The slow-moving component was found to be moving with subsonic velocities. Optical emission spectroscopy showed that the slower moving component is contributed by nanoparticles, whereas the fast-moving component is comprised of U I, UO and U_xO_y molecules.

2D spectral images were taken to investigate spatio-temporal evolution of U plumes in 700 Torr air. Spectral imaging highlighted the progression from atoms (U) to diatoms (UO) to polyatomic molecules (U_xO_y), and associated hydrodynamics of the plume. At early times, the continuum and U atomic emission are dominant. The broad spectral features of UO centred at 593.55 nm are seen even at ~1 µs. Time-resolved 2D spectral imaging also reveals U I, UO, and U_xO_y co-exist within the fast-moving component of the plume up to 16 µs, and at later times this faster component is entirely comprised of higher oxides. We attribute the early time appearance of molecular emission and co-location of atoms and molecules within the plume to the lower temperature conditions in filament produced plasmas, in comparison to those in ns LPPs. The emission from the filament generated plasma at the end of its lifetime is found to be comprised of nanoparticles.

The broad molecular (UO and U_XO_Y) spectral features seen in the present measurement are due to convolution of numerous transitions. It should also be mentioned that for molecules with large moments of inertia (such as UO), the rotational levels become more closely spaced and may be difficult to resolve using standard emission-based passive techniques (e.g. LIBS) used in the present study. Extremely high resolution and active sensing spectroscopic tools such as laser absorption spectroscopy, laser-induced fluorescence, or frequency comb spectroscopy of plasmas[63] may be useful for resolving these finer structures of UO molecular emission.

Conflicts of interest

There are no conflicts to declare.

Acknowledgements

The authors acknowledge the U.S. Department of Energy/NNSA Office of Defense Nuclear Nonproliferation for financial support under contract DE-NA0002534. The work presented here was performed at Pacific Northwest National Laboratory, which is operated for the U.S. DOE by Battelle Memorial Institute under Contract No. DE-AC05-76RLO1830.

References

1. J. P. Singh and S. N. Thakur, *Laser induced breakdown spectroscopy*, Elsevier, Amsterdam, 2007.
2. S. Musazzi and U. Perini, *Laser-Induced Breakdown Spectroscopy – Fundamentals and Applications* Springer Series in Optical Sciences2014.
3. S. S. Harilal, B. E. Brumfield, N. L. LaHaye, K. C. Hartig and M. C. Phillips, *Applied Physics Reviews*, 2018, **5**, 021301.
4. L. A. Finney, P. J. Skrodzki, M. Burger, J. Nees, S. S. Harilal and I. Jovanovic, *Optics Letters*, 2019, **44**, 2783.
5. J. Wu, Y. Qiu, X. W. Li, H. Yu, Z. Zhang and A. C. Qiu, *J Phys D Appl Phys*, 2020, **53**, 023001.
6. R. C. Wiens, S. Maurice, B. Barraclough, M. Saccoccio, W. C. Barkley, J. F. Bell, S. Bender, J. Bernardin, D. Blaney, J. Blank, M. Bouyé, N. Bridges, N. Bultman, P. Caïs, R. C. Clanton, B. Clark, S. Clegg, A. Cousin, D. Cremers, A. Cros, L. DeFlores, D. Delapp, R. Dingler, C. D'Uston, M. Darby Dyar, T. Elliott, D. Enemark, C. Fabre, M. Flores, O. Forni, O. Gasnault, T. Hale, C. Hays, K. Herkenhoff, E. Kan, L. Kirkland, D. Kouach, D. Landis, Y. Langevin, N. Lanza, F. LaRocca, J. Lasue, J. Latino, D. Limonadi, C. Lindensmith, C. Little, N. Mangold, G. Manhes, P. Mauchien, C. McKay, E. Miller, J. Mooney, R. V. Morris, L. Morrison, T. Nelson, H. Newsom, A. Ollila, M. Ott, L. Pares, R. Perez, F. Poitrasson, C. Provost, J. W. Reiter, T. Roberts, F. Romero, V. Sautter, S. Salazar, J. J. Simmonds, R. Stiglich, S. Storms, N. Striebig, J.-J. Thocaven, T. Trujillo, M. Ulibarri, D. Vaniman, N.

Warner, R. Waterbury, R. Whitaker, J. Witt and B. Wong-Swanson, *Space Science Reviews*, 2012, **170**, 167-227.
7. C. Kimblin, R. Trainham, G. A. Capelle, X. L. Mao and R. E. Russo, *Aip Adv*, 2017, **7**, 095208.
8. J. L. Gottfried, *Physical Chemistry Chemical Physics*, 2014, **16**, 21452-21466.
9. S. A. Irimiciuc, P.-E. Nica, M. Agop and C. Focsa, *Appl Surf Sci*, 2020, **506**, 144926.
10. D. W. Hahn and N. Omenetto, *Applied Spectroscopy*, 2012, **66**, 347-419.
11. D. W. Hahn and N. Omenetto, *Applied Spectroscopy*, 2010, **64**, 335a-366a.
12. B. N. Chichkov, C. Momma, S. Nolte, F. vonAlvensleben and A. Tunnermann, *Appl Phys a-Mater*, 1996, **63**, 109-115.
13. S. Sunku, M. K. Gundawar, A. K. Myakalwar, P. P. Kiran, S. P. Tewari and S. V. Rao, *Spectrochimica Acta Part B: Atomic Spectroscopy*, 2013, **79**, 31-38.
14. J. Serrano, J. Moros and J. J. Laserna, *Physical Chemistry Chemical Physics*, 2016, **18**, 2398-2408.
15. V. Margetic, A. Pakulev, A. Stockhaus, M. Bolshov, K. Niemax and R. Hergenroder, *Spectrochim Acta B*, 2000, **55**, 1771-1785.
16. S. A. Kalam, N. L. Murthy, P. Mathi, N. Kommu, A. K. Singh and S. V. Rao, *Journal of Analytical Atomic Spectrometry*, 2017, **32**, 1535-1546.
17. E. G. Gamaly, *Femtosecond Laser-Matter Interaction: Theory, Experiments and Applications* Pan Stanford, Singapore, 2011.
18. E. L. Gurevich and R. Hergenroder, *Applied Spectroscopy*, 2007, **61**, 233A-242A.
19. K. C. Hartig, I. Ghebregziabher and I. Jovanovic, *Scientific Reports*, 2017, **7**, 43852.
20. M. C. Phillips, B. E. Brumfield, N. LaHaye, S. S. Harilal, K. C. Hartig and I. Jovanovic, *Scientific Reports*, 2017, **7**, 3784.
21. S. L. Chin, *Femtosecond Laser Filamentation*, Springer-Verlag New York, 2010.
22. T. A. Labutin, V. N. Lednev, A. A. Ilyin and A. M. Popov, *Journal of Analytical Atomic Spectrometry*, 2016, **31**, 90-118.
23. K. Stelmaszczyk, P. Rohwetter, G. Méjean, J. Yu, E. Salmon, J. Kasparian, R. Ackermann, J.-P. Wolf and L. Wöste, *Appl. Phys. Lett.*, 2004, **85**, 3977-3979.
24. M. Durand, A. Houard, B. Prade, A. Mysyrowicz, A. Durecu, B. Moreau, D. Fleury, O. Vasseur, H. Borchert, K. Diener, R. Schmitt, F. Theberge, M. Chateauneuf, J. F. Daigle and J. Dubois, *Opt Express*, 2013, **21**, 26836-26845.
25. P. Rohwetter, K. Stelmaszczyk, L. Wöste, R. Ackermann, G. Méjean, E. Salmon, J. Kasparian and J.-P. Wolf, *Spectrochim. Acta, Part B*, 2005, **60**, 1025-1033.
26. S. S. Harilal, J. Yeak and M. C. Phillips, *Optics Express*, 2015, **23**, 27113.
27. X. L. Liu, X. Lu, X. Liu, T. T. Xi, F. Liu, J. L. Ma and J. Zhang, *Opt Express*, 2010, **18**, 26007-26017.
28. P. P. Kiran, S. Bagchi, C. L. Arnold, S. R. Krishnan, G. R. Kumar and A. Couairon, *Opt Express*, 2010, **18**, 21504-21510.
29. S. S. Harilal, J. Yeak, B. E. Brumfield and M. C. Phillips, *Journal of Analytical Atomic Spectrometry*, 2016, **31**, 1192-1197.
30. S. S. Harilal, J. Yeak, B. E. Brumfield and M. C. Phillips, *Optics Express*, 2016, **24**, 17941.
31. S. S. Harilal, E. J. Kautz, B. E. Bernacki, M. C. Phillips, P. Skrodzki, M. Burger and I. Jovanovic, *Physical Chemistry Chemical Physics*, 2019, **21**, 16161.
32. E. J. Kautz, P. Skrodzki, M. Burger, I. Jovanovic, B. E. Bernacki, M. C. Phillips and S. S. Harilal, *Journal of Analytical Atomic Spectrometry*, 2019, **34**, 2236-2243.
33. S. S. Harilal, T. Sizyuk, A. Hassanein, D. Campos, P. Hough and V. Sizyuk, *Journal of Applied Physics*, 2011, **109**, 063306.
34. Y. B. Zeldovich and Y. P. Raizer, *Physics of shock waves and high-temperature hydrodynamic phenomena*, Dover, New York, 2001.
35. P. Skrodzki, M. Burger, I. Jovanovic, B. E. Brumfield, M. C. Phillips and S. S. Harilal, *Optics Letters*, 2018, **43**, 5118.
36. S. S. Harilal, B. E. Brumfield, N. Glumac and M. C. Phillips, *Optics Express*, 2018, **26**, 20319.
37. S. S. Harilal, N. Farid, A. Hassanein and V. M. Kozhevin, *Journal of Applied Physics*, 2013, **114**, 203302.
38. P. J. Skrodzki, M. Burger, I. Jovanovic, M. C. Phillips, J. Yeak, B. E. Brumfield and S. S. Harilal, *Physics of Plasmas*, 2019, **26**, 083508.
39. J. Siegel, G. Epurescu, A. Perea, F. J. Gordillo-Vazquez, J. Gonzalo and C. N. Afonso, *Optics Letters*, 2004, **29**, 2228-2230.
40. K. K. Anoop, X. C. Ni, M. Bianco, D. Paparo, X. Wang, R. Bruzzese and S. Amoruso, *Appl Phys a-Mater*, 2014, **117**, 313-318.
41. C. Focsa, S. Gurlui, P. Nica, M. Agop and M. Ziskind, *Appl Surf Sci*, 2017, **424**, 299-309.
42. J. R. Freeman, S. S. Harilal, P. K. Diwakar, B. Verhoff and A. Hassanein, *Spectrochimica Acta Part B-Atomic Spectroscopy*, 2013, **87**, 65-73.
43. B. Verhoff, S. S. Harilal, J. R. Freeman, P. K. Diwakar and A. Hassanein, *Journal of Applied Physics*, 2012, **112**, 093303.
44. J. Guo, J. Shao, T. Wang, C. Zheng, A. Chen and M. Jin, *Journal of Analytical Atomic Spectrometry*, 2017, **32**, 367-372.
45. S. S. Harilal, C. V. Bindhu, M. S. Tillack, F. Najmabadi and A. C. Gaeris, *Journal of Physics D: Applied Physics*, 2002, **35**, 2935-2938.
46. H. Hou, B. Yang, X. Mao, V. Zorba, P. Ran and R. E. Russo, *Opt. Express*, 2018, **26**, 13425-13435.
47. S. S. Harilal, *Journal of Applied Physics*, 2007, **102**, 123306.
48. K. K. Anoop, M. P. Polek, R. Bruzzese, S. Amoruso and S. S. Harilal, *Journal of Applied Physics*, 2015, **117**, 083108.
49. K. K. Anoop, S. S. Harilal, R. Philip, R. Bruzzese and S. Amoruso, *Journal of Applied Physics*, 2016, **120**, 185901.
50. S. S. Harilal, R. C. Issac, C. V. Bindhu, V. P. N. Nampoori and C. P. G. Vallabhan, *Journal of Applied Physics*, 1997, **81**, 3637-3643.
51. B. Campanella, S. Legnaioli, S. Pagnotta, F. Poggialini and V. Palleschi, *Atoms*, 2019, **7**, 57.
52. S. S. Harilal, C. V. Bindhu, M. S. Tillack, F. Najmabadi and A. C. Gaeris, *Journal of Applied Physics*, 2003, **93**, 2380-2388.
53. T. L. Martin, C. Coe, P. A. J. Bagot, P. Morrall, G. D. W. Smith, T. Scott and M. P. Moody, *Sci Rep-Uk*, 2016, **6**, 25618.
54. D. G. Weisz, J. C. Crowhurst, M. S. Finko, T. P. Rose, B. Koroglu, R. Trappitsch, H. B. Radousky, W. J. Siekhaus, M. R. Armstrong, B. H. Isselhardt, M. Azer and D. Curreli, *Journal of Physical Chemistry A*, 2018, **122**, 1584-1591.

55. X.-L. Zeng, S.-Q. Huang and X.-H. Ju, *Journal of Radioanalytical and Nuclear Chemistry*, 2013, **298**, 481-484.
56. M. S. Finko, D. Curreli, D. G. Weisz, J. C. Crowhurst, T. P. Rose, B. Koroglu, H. B. Radousky and M. R. Armstrong, *Journal of Physics D: Applied Physics*, 2017, **50**, 485201.
57. M. S. Finko and D. Curreli, *Phys Plasmas*, 2018, **25**, 083112.
58. P. J. Skrodzki, N. Shah, N. Taylor, K. Hartig, N. LaHaye, B. Brumfield, I. Jovanovic, M. C. Phillips and S. S. Harilal, *Spectrochimica Acta Part B-Atomic Spectroscopy*, 2016, **125** 112–119.
59. L. A. Kaledin, E. A. Shenyavskaya and L. V. Gurvich, *Russian J. Phys. Chem.*, 1986, **60**, 633.
60. J. D. Han, V. Goncharov, L. A. Kaledin, A. V. Komissarov and M. C. Heaven, *Journal of Chemical Physics*, 2004, **120**, 5155-5163.
61. S. D. Zhang, X. H. Wang, M. H. He, Y. B. Jiang, B. C. Zhang, W. Hang and B. L. Huang, *Spectrochim Acta B*, 2014, **97**, 13-33.
62. N. M. Shaikh, M. S. Kalhoro, A. Hussain and M. A. Baig, *Spectrochim Acta B*, 2013, **88**, 198-202.
63. J. Bergevin, T.-H. Wu, J. Yeak, B. E. Brumfield, S. S. Harilal, M. C. Phillips and R. J. Jones, *Nature Communications*, 2018, **9**, 1273.
64. S. Amoruso, G. Ausanio, R. Bruzzese, M. Vitiello and X. Wang, *Physical Review B*, 2005, **71**, 033406.
65. S. Noël, J. Hermann and T. Itina, *Applied Surface Science*, 2007, **253**, 6310-6315.

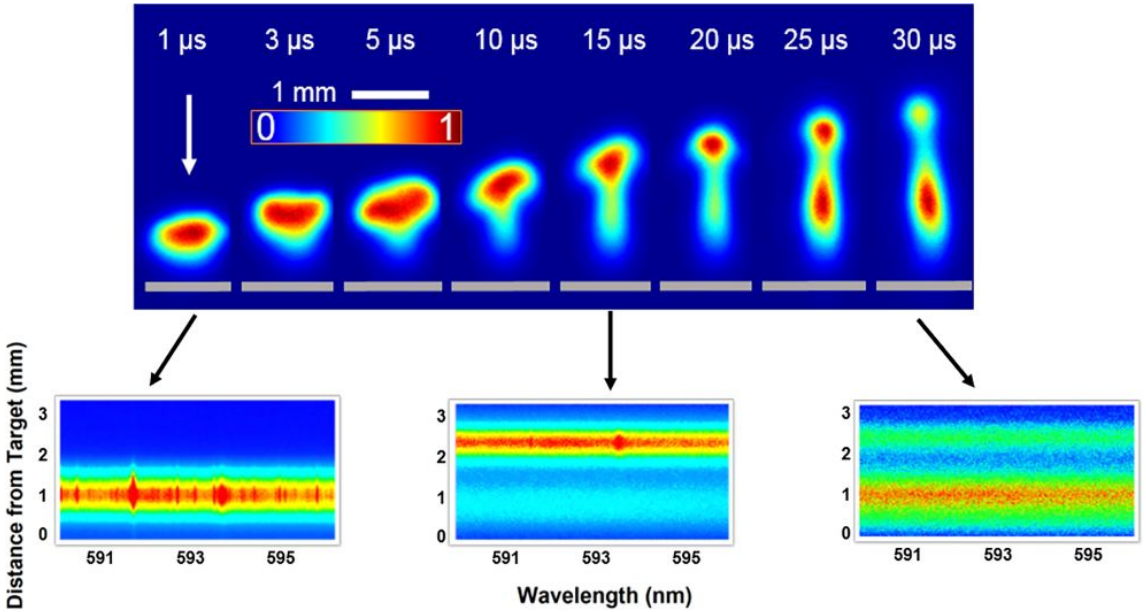

Table of Contents Entry

Caption: 2D plume and spectral imaging illustrate expansion dynamics and corresponding chemical evolution of atoms and molecules in filament produced plasmas